Supporting Information for

# A Flexible Tribotronic Artificial Synapse with Bioinspired Neurosensory Behavior

Jianhua Zeng[1, 2, †], Junqing Zhao[1, 3, †], Tianzhao Bu[1, 3], Guoxu Liu[1, 3], Youchao Qi[1, 3], Han Zhou[1, 2], Sicheng Dong[1, 3], Chi Zhang[1, 2, 3, *]

[1] CAS Center for Excellence in Nanoscience, Beijing Key Laboratory of Micro-nano Energy and Sensor, Beijing Institute of Nanoenergy and Nanosystems, Chinese Academy of Sciences, Beijing 101400, P. R. China

[2] Center on Nanoenergy Research, School of Physical Science and Technology, Guangxi University, Nanning, 530004, P. R. China

[3] School of Nanoscience and Technology, University of Chinese Academy of Sciences, Beijing 100049, P. R. China

[†]Jianhua Zeng and Junqing Zhao contributed equally to this work.

*Corresponding author. E-mail: czhang@binn.cas.cn (Chi Zhang)

## Supplementary Figures and Tables
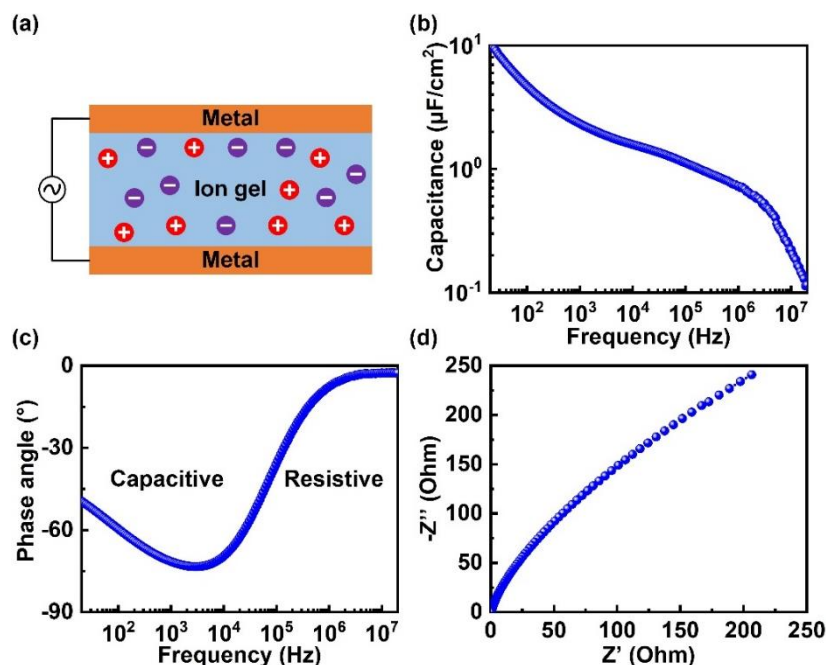


**Fig. S1** Impedance analysis of the ion-gel dielectric film. (**a**) Typical MIM structure diagram of the ion-gel dielectric film. (**b**) The functional relationship between the capacitance of the ion-gel dielectric film and the frequency of applied AC. (**c**) The functional relationship between the phase angle of the ion-gel dielectric film and the frequency of applied AC. (**d**) Nyquist plot of the ion-gel dielectric film
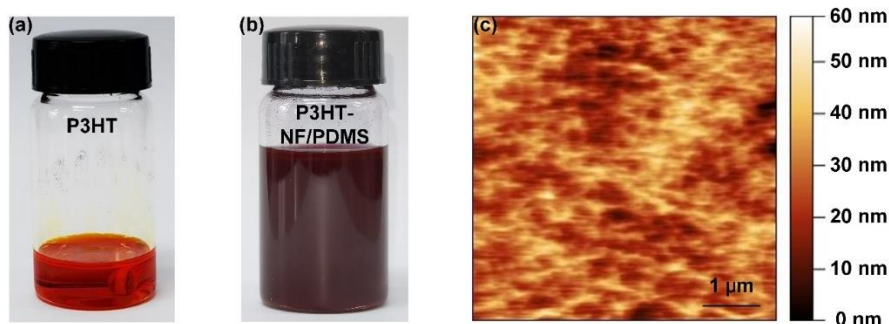
**Fig. S2** Characterization of the P3HT-NF/PDMS semiconductor. (**a**) Optical image after complete dissolution of P3HT. (**b**) Optical image of the P3HT-NF/PDMS semiconductor solution. (**c**) The AFM morphology of the P3HT-NF/PDMS semiconductor film
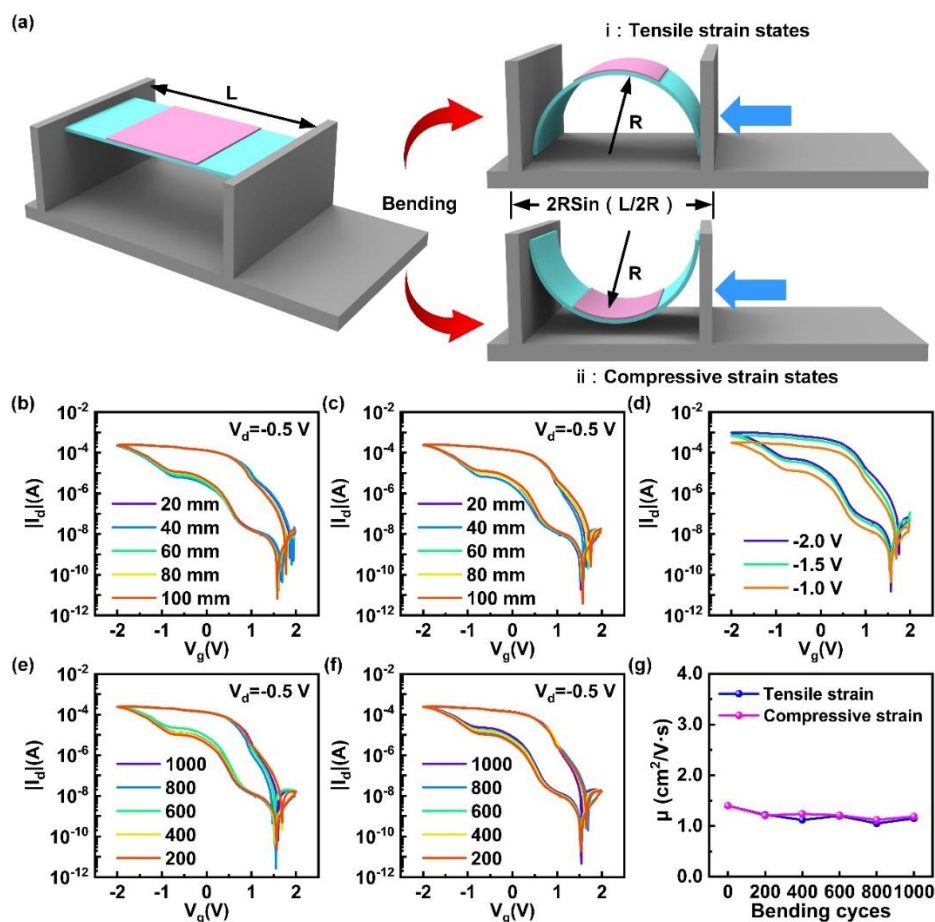


**Fig. S3** The bending process diagram and electrical characteristics of the OTFT. (**a**) Schematic illustration of the OTFT in tensile and compressive strain states, respectively. (**b**) Double-sweep transfer characteristics of the OTFT under different bending radius in tensile strain states. (**c**) Double-sweep transfer characteristics of the OTFT under different bending radius in compressive strain states. (**d**) Double-sweep transfer characteristics of the OTFT under different $V_d$. (**e**) Double-sweep transfer characteristics of the OTFT after different number of tensile strain cycles with a bending radius of 20 mm. (**f**) Double-sweep transfer characteristics of the OTFT after different number of compressive strain cycles with a bending radius of 20 mm. (**g**) The mobility of the OTFT after different number of tensile and compressive strain cycles with a bending radius of 20 mm
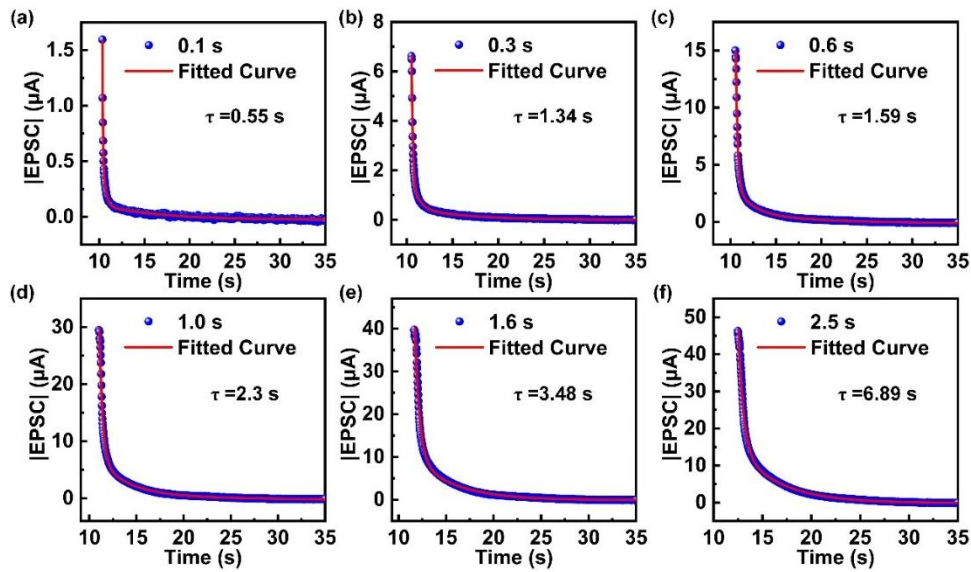
**Fig. S4** The fitting of the EPSC decay behavior with stretched-exponential decay model. (**a-f**) The fitting of the EPSC decay behavior with stretched-exponential decay model under single mechanical stimuli with different duration time (0.1 s, 0.3 s, 0.6 s, 1.0 s, 1.6 s and 2.5 s)
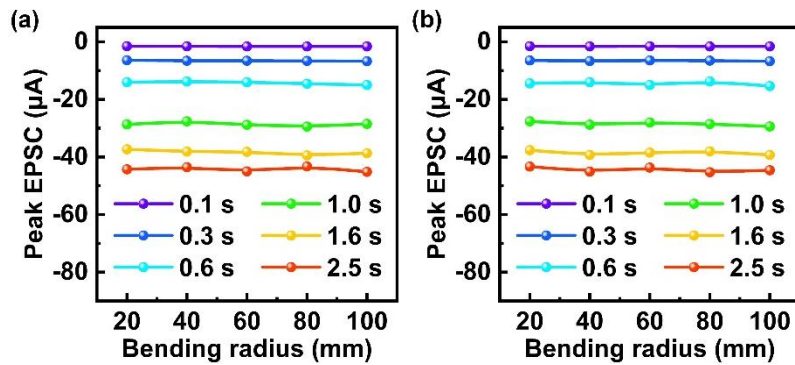


**Fig. S5** The effect of different bending radius on EPSC peak value of the TAS under single mechanical stimuli with different duration time. (**a**) The effect of different bending radius in tensile strain states on EPSC peak value of the TAS under single mechanical stimuli with different duration time. (**b**) The effect of different bending radius in compressive strain states on EPSC peak value of the TAS under single mechanical stimuli with different duration time
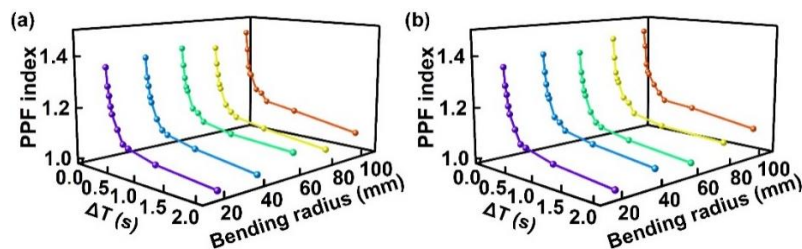


**Fig. S6** The effect of different bending radius on PPF index of the TAS under paired mechanical stimuli with different interval time. (**a**) The effect of different bending radius in tensile strain states on PPF index of the TAS under paired mechanical stimuli with different interval time. (**b**) The effect of different bending radius in compressive strain states on PPF index of the TAS under paired mechanical stimuli with different interval time.
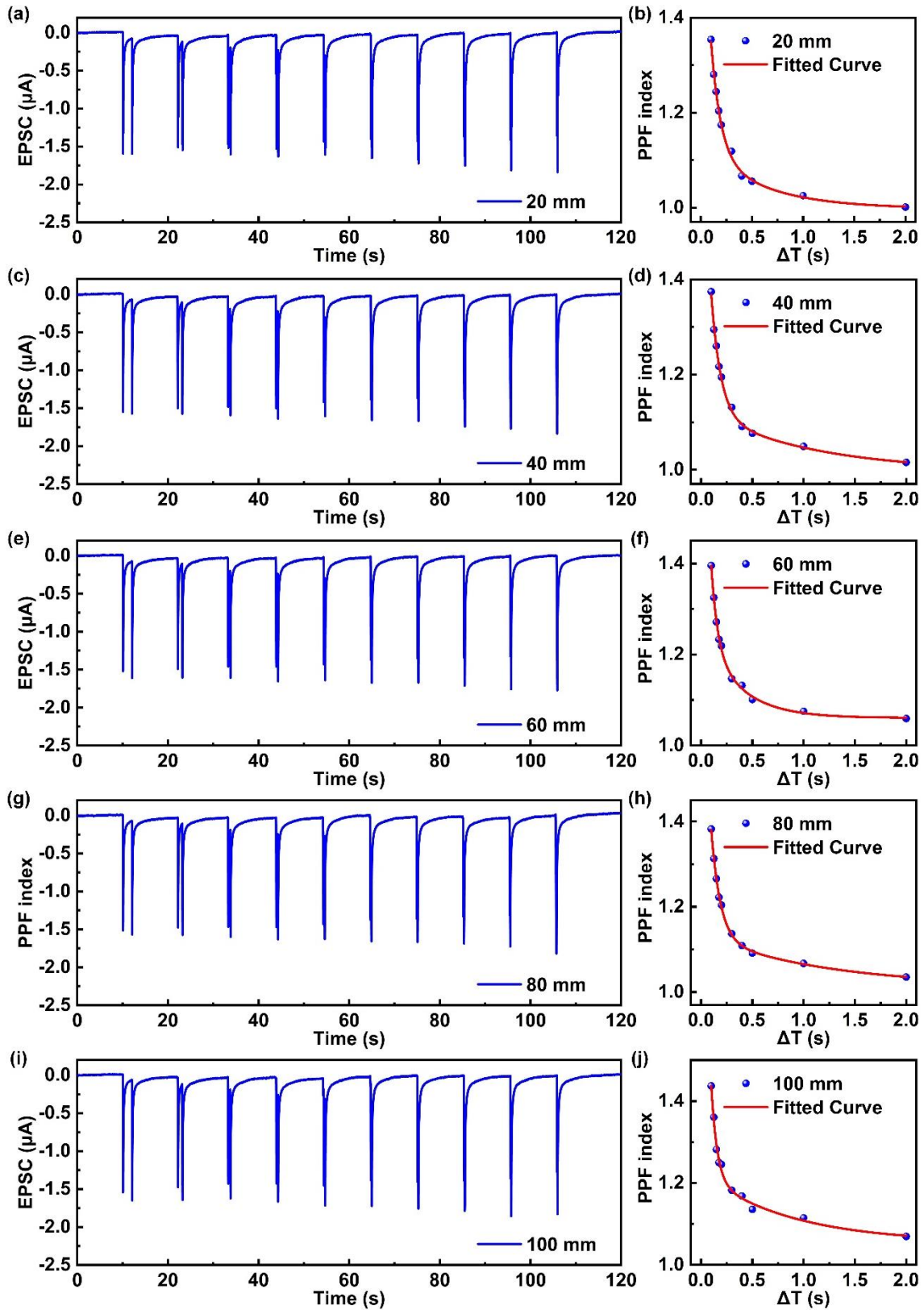
**Fig. S7** EPSC and PPF index response of the TAS under different bending radius in tensile strain states. (**a**), (**c**), (**e**), (**g**) and (**i**) The EPSC response of the TAS under different bending radius (20, 40, 60, 80 and 100 mm) in tensile strain states, respectively. (**b**), (**d**), (**f**), (**h**) and (**j**) The PPF index response of the TAS under different bending radius (20, 40, 60, 80 and 100 mm) in tensile strain states
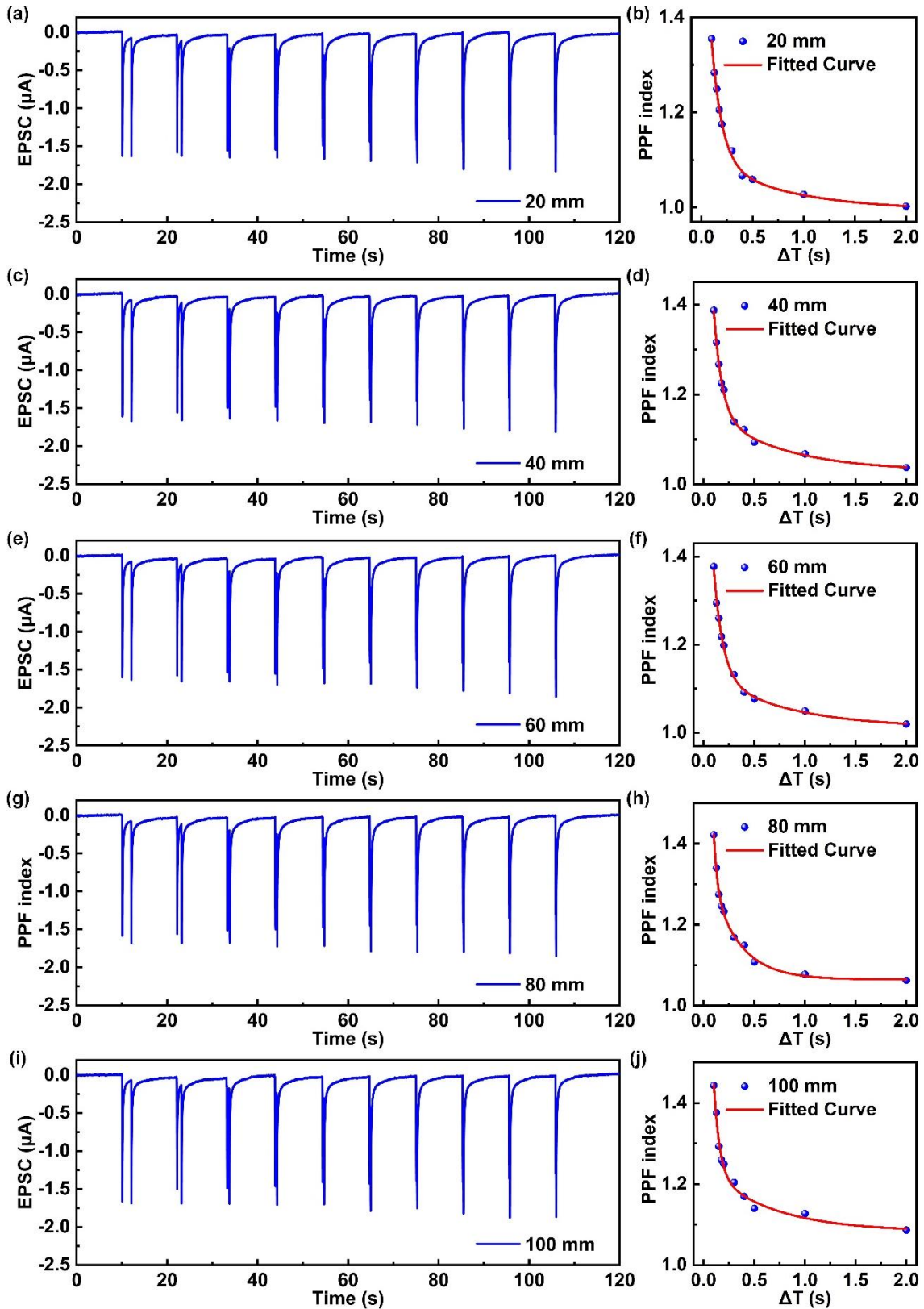
**Fig. S8** The EPSC and PPF index response of the TAS under different bending radius in compressive strain states. (**a**), (**c**), (**e**), (**g**) and (**i**) The EPSC response of the TAS under different bending radius (20, 40, 60, 80 and 100 mm) in compressive strain states, respectively. (**b**), (**d**), (**f**), (**h**) and (**j**) The PPF index response of the TAS under different bending radius (20, 40, 60, 80 and 100 mm) in compressive strain states, respectively.
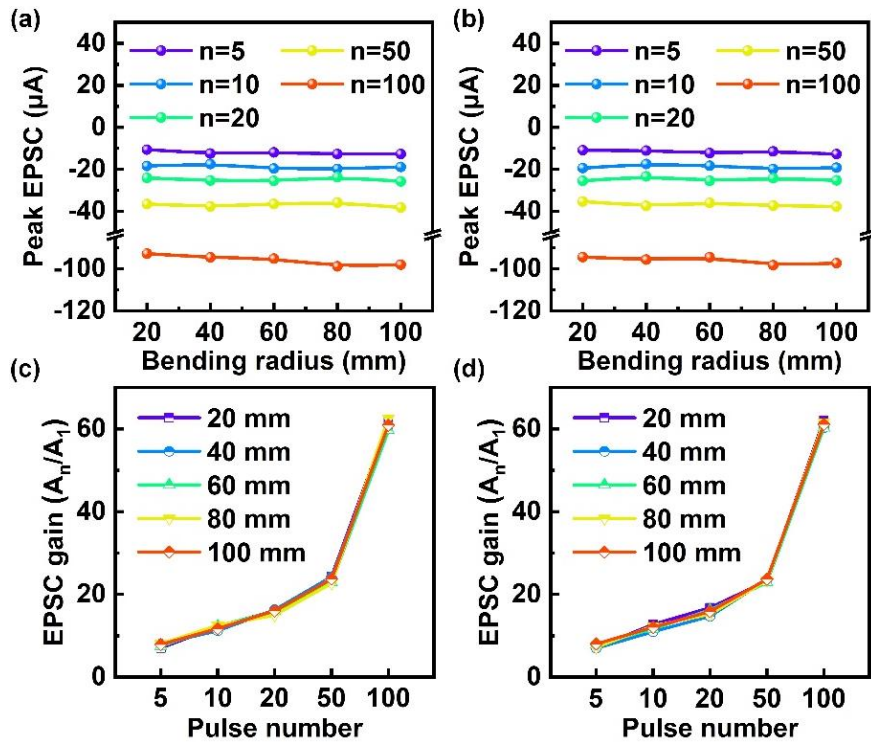
**Fig. S9** The effect of different bending radius on the output characteristics of the TAS under multiple mechanical stimuli with a duration time of 0.1 s. (**a**) The effect of different bending radius in tensile strain states on the EPSC peak value of the TAS under multiple mechanical stimuli with a duration time of 0.1 s. (**b**) The effect of different bending radius in compressive strain states on the EPSC peak value of the TAS under multiple mechanical stimuli with a duration time of 0.1 s. (**c**) The effect of the different bending radius in tensile strain states on the EPSC gain of the TAS (EPSC gain is defined as $A_n/A_1$) under multiple continuous mechanical stimuli with a duration time of 0.1 s. (**d**) The effect of the different bending radius in compressive strain states on the EPSC gain of the TAS (EPSC gain is defined as $A_n/A_1$) under multiple continuous mechanical stimuli with a duration time of 0.1 s
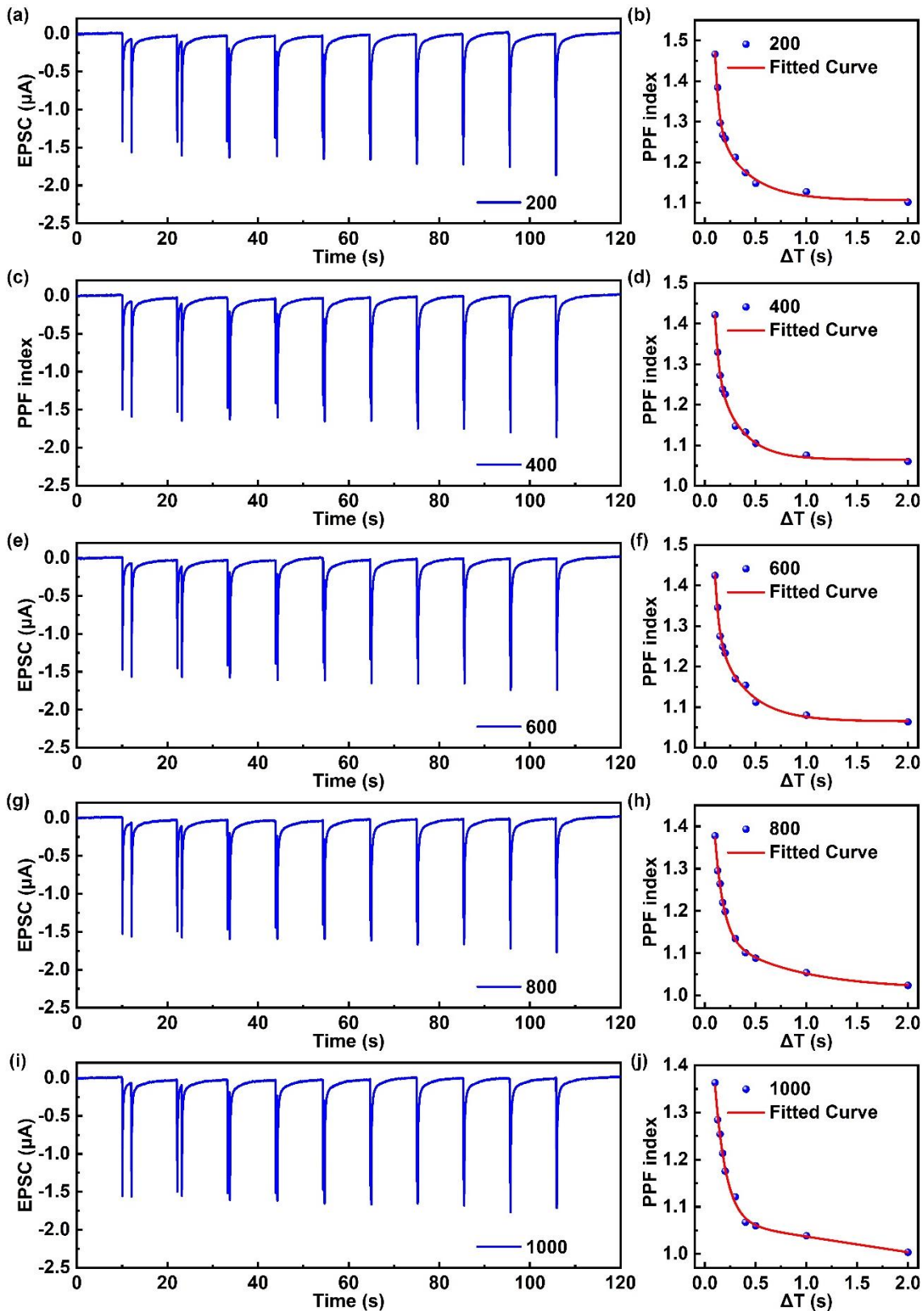
**Fig. S10** EPSC and PPF index response of the TAS after tensile strain cycles with bending radius of 20 mm. (**a**), (**c**), (**e**), (**g**) and (**i**) The EPSC response of the TAS after different tensile strain cycles (200, 400, 600, 800 and 1000) with bending radius of 20 mm, respectively. (**b**), (**d**), (**f**), (**h**) and (**j**) The EPSC response of the TAS after different tensile strain cycles (200, 400, 600, 800 and 1000) with bending radius of 20 mm
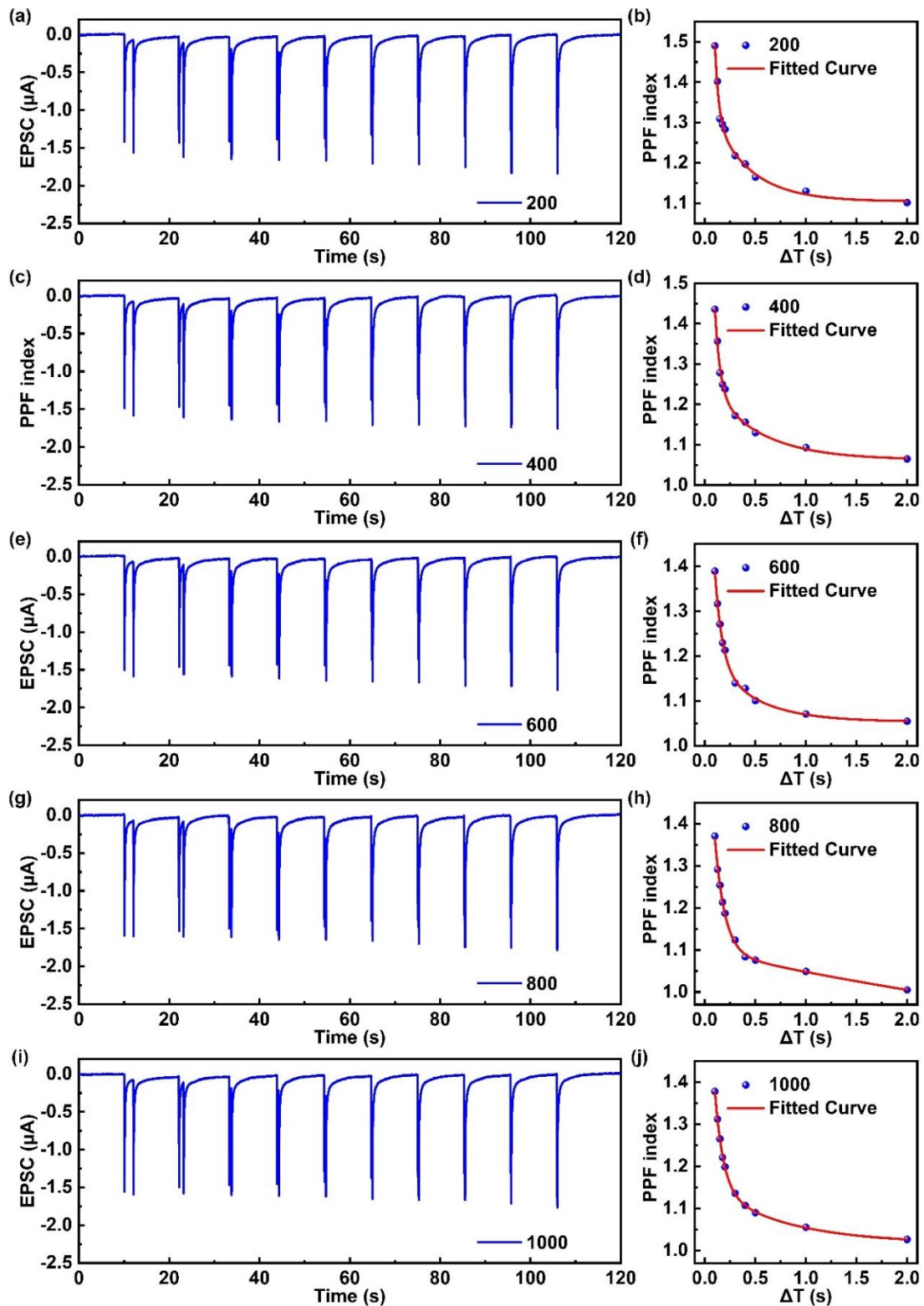
**Fig. S11.** The EPSC and PPF index responses of the TAS after compressive strain cycles with bending radius of 20 mm. (**a**), (**c**), (**e**), (**g**) and (**i**) The EPSC response of the TAS after different compressive strain cycles (200, 400, 600, 800 and 1000) with bending radius of 20 mm, respectively. (**b**), (**d**), (**f**), (**h**) and (**j**) The EPSC response of the TAS after different compressive strain cycles (200, 400, 600, 800 and 1000) with bending radius of 20 mm
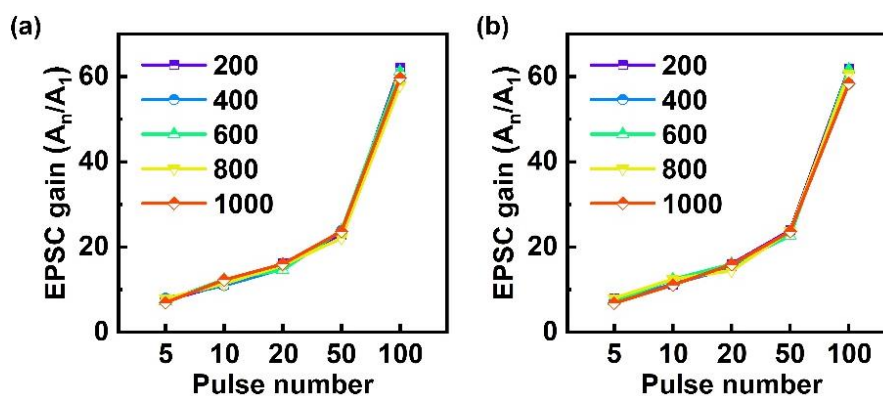
**Fig. S12** The effect of the number of tensile and compressive strain cycles with a bending radius of 20 mm on the EPSC gain of the TAS (EPSC gain is defined as $A_n/A_1$) under multiple continuous mechanical stimuli with a duration time of 0.1 s. (**a**) The effect of the number of tensile strain cycles with a bending radius of 20 mm on the EPSC gain of the TAS under multiple continuous mechanical stimuli with a duration time of 0.1 s. (**b**) The effect of the number of compressive strain cycles with a bending radius of 20 mm on the EPSC gain of the TAS under multiple continuous mechanical stimuli with a duration time of 0.1 s

**Table S1** The comparison of the reported artificial synapses in previous literature

| Activation modes | Substrate | Electrodes | Active layer | Dielectric layer | Stimuli signal | EPSC Decay time | PPF $A^2/A^1$ | SM to LTM Retention time | Refs. |
|---|---|---|---|---|---|---|---|---|---|
| External power | ITO glass | IZO | IZO | Chitosan | Electrical pulse | N/A | ~1.36 | 8 s | [S1] |
| Piezoelectric | PET | Cr/Au | Graphene | PEGDA+HOMPP EMIM-TFSI | Force | 3.24 s | ~1.4 | — | [S2] |
| Triboelectric | Si | Cr/Au | $MoS_2$ | PSSH | Force | N/A | 1.16 | — | [S3] |
| | Si | Cr/Au | $MoS_2$ | PEGDA+HOMPP EMIM-TFSI | Force | 75 ms | ~1.4 | ~10 s | [S4] |
| | PET | Ti/Au | P3HT-NF/PDMS | PVDF-HFP +EMIM-TFSI | Force / Vibration | 6.89 s | 1.56 | 30 s | This work |

# Supplementary References

[S1] J. Zhou, Y. Liu, Y. Shi, Q. Wan, Solution-processed chitosan-gated IZO-based transistors for mimicking synaptic plasticity. Ieee Electr. Device L. **35**(2), 280-282(2014). https://doi.org/10.1109/LED.2013.2295815

[S2] Y. Chen, G. Gao, J. Zhao, H. Zhang, J. Yu et al., Piezotronic graphene artificial sensory synapse. Adv. Funct. Mater. **29**(41), 1900959(2019). https://doi.org/10.1002/adfm.201900959

[S3] X. Yang, J. Han, J. Yu, Y. Chen, H. Zhang et al., Versatile triboiontronic transistorvia proton conductor. ACS Nano **14**(7), 8668-8677(2020). https://doi.org/10.1021/acsnano.0c03030

[S4] J. Yu, G. Gao, J. Huang, X. Yang, J. Han et al., Contact-electrification-activated artificial afferents at femtojoule energy. Nat. Commun. **12**(1), 1581(2021). https://doi.org/10.1038/s41467-021-21890-1